Regular Article

The design of high performance photoanode of CQDs/TiO₂/WO₃ based on DFT alignment of lattice parameter and energy band, and charge distribution

Jiachen Wang [a], Tingsheng Zhou [a], Yan Zhang [a], Shuai Chen [a], Jing Bai [a], Jinhua Li [a], Hong Zhu [b,**], Baoxue Zhou [a,c,*]

[a] School of Environmental Science and Engineering, Key Laboratory of Thin Film and Microfabrication Technology (Ministry of Education), Shanghai Jiao Tong University, Shanghai 200240, PR China
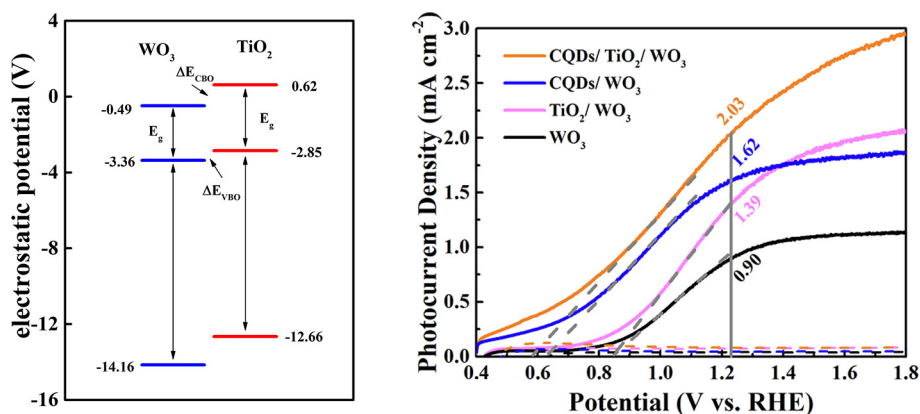[b] University of Michigan – Shanghai Jiao Tong University Joint Institute, Shanghai Jiao Tong University, Shanghai 200240, PR China
[c] Shanghai Institute of Pollution Control and Ecological Security, Shanghai 200092, PR China

HIGHLIGHTS

- CQDs/TiO₂/WO₃ is designed on the basis of dual alignment and charge distribution.
- TiO₂ epitaxially grow on WO₃ with ~3% lattice mismatch to form heterojunction.
- The built-in field of TiO₂/WO₃ can inhibit bulk recombination with band alignment.
- CQDs can extend visible light absorption and shift onset potential cathodically.
- PEC water splitting performance of CQDs/TiO₂/WO₃ has been significantly improved.

GRAPHICAL ABSTRACT

ARTICLE INFO

ABSTRACT

Photoanode is the key issue for photoelectrocatalytic (PEC) water splitting and organics degradation. However, it always faces several restrictions including severe photocorrosion, low charge separation and transfer efficiencies, poor visible light harvesting, and sluggish interfacial reaction kinetics, which often required a variety of modifications with only low improvements achieved. Herein, a high performance CQDs/TiO₂/WO₃ photoanode was designed on the basis of density function theory (DFT) alignment of lattice parameters and energy band, and charge distribution. The TiO₂/WO₃ heterojunction can abate photocorrosion through the hetero-epitaxial growth of TiO₂ (0 0 1) on WO₃ (0 0 2) for the lattice mismatch <3% eliminating dangling bonds, with high corrosion resistance and photostability of TiO₂. As the built-in field constructed by a staggered band alignment structure with the valence band offset (VBO) of 0.51 eV, the photogenerated carriers transfer and separation are promoted dramatically. Through the DFT calculations, the sunlight absorption wavelength can be extended, and the interfacial reaction kinetics can be expedited with the modification of carbon quantum dots (CQDs) on TiO₂/WO₃, due to the narrower

---

* Corresponding author at: School of Environmental Science and Engineering, Shanghai Jiao Tong University.
** Corresponding author at: University of Michigan – Shanghai Jiao Tong University Joint Institute, Shanghai Jiao Tong University.
  E-mail addresses: hong.zhu@sjtu.edu.cn (H. Zhu), zhoubaoxue@sjtu.edu.cn (B. Zhou).

bandgap (E_g) and the accumulation of electrons at TiO$_2$ side. The DFT designed CQDs/TiO$_2$/WO$_3$ photoanode significantly increase photocurrent density from 0.90 to 2.03 mA cm^{-2} at 1.23 V, charge separation efficiency from 56.3 to 79.2% and charge injection efficiency from 51.2 to 70.4%, and extend light absorption edge from 455 to 463 nm over pristine WO$_3$, with better photostability and lower holes-to-water resistance.

1. Introduction

Metal-oxide semiconductors are efficiently investigated to degrade organic pollutants and split water to generate hydrogen by PEC method, which is a prospective and sustainable strategy to converse solar energy and overcome the growing environmental problems [1–3]. The highly active semiconductors, such as WO$_3$, TiO$_2$, Fe$_2$O$_3$ and BiVO$_4$, have been studied in a deep-going way by many researchers [4–8]. However, severe photocorrosion, low charge separation and transfer efficiency, sluggish reaction kinetics, and insufficient sunlight absorption are always the focus of PEC process. For example, WO$_3$ is low cost and chemical stable in acidic condition, has an appropriate hole diffusion length (~150 nm) [9–12], but suffers from the severe photocorrosion to generate peroxo species, sluggish holes transfer kinetics and rapid recombination of photoexcited carriers [13–15]. And TiO$_2$ owns the advantages of nontoxicity, abundant storage and good stability under a variety of conditions, but its larger bandgap results in only ultraviolet response with insufficient utilization of sunlight [16–18].

To improve the photocatalytic or PEC conversion performance, constructing a heterojunction with two semiconductors may address the concentrated issues, overcoming the intrinsic shortcomings of materials. Various heterojunctions have been reported to improve photostability, or to enhance spatial separation of hole-electron pairs by the generated built-in electric field, such as Bi$_2$S$_3$/WO$_3$ [19], MoS$_2$/ZnO [20], ZnWO$_4$/WO$_3$ [21], C$_3$N$_4$/ZnO [22], and Cu$_2$O/TiO$_2$/Bi$_2$O$_3$ [23]. In addition, several studies have reported that epitaxial growth is beneficial from the lattice-matched materials, for example, CuO/MgO [24], TiO$_2$/SrTiO$_3$ [25], and g-C$_3$N$_4$/graphene [26]. Possible epitaxial growth of TiO$_2$/WO$_3$ heterojunction based on matched lattice, has been proposed in our previous work [4], revealing the advantages of good photostability and rapid charge carriers separation.

Since the TiO$_2$-based heterojunction cannot enhance the visible absorption, CQDs as a promising photoelectric material could extend the visible light harvesting range, with many advantages of eco-friendliness, low cost, simple synthesis, chemical inertness and up-conversion photoluminescence (PL) properties [16,27–31]. Furthermore, CQDs can form heterojunctions with some metal oxide semiconductors accelerating the holes transfer to the electrode surface, such as CQDs/Fe$_2$O$_3$ [32], CQDs/BiVO$_4$ [27], CQDs/WO$_3$ [33], CQDs/ZnO [34] and CQDs/TiO$_2$ [35–37], etc. Due to small particle sizes of CQDs, they possess highly photo-luminescent emissions, photo-induced electrons transfer and excellent properties as semiconductor nanoparticles for photo-catalysis, supercapacitor and visible light sensitizer [38]. And CQDs could function as an ultrafast charge channel to promote the charge injection efficiency, and shift the onset potential cathodically [39,40].

In this paper, a high performance photoanode of CQDs/TiO$_2$/WO$_3$ was designed and prepared on the basis of DFT alignment of lattice parameters and energy band, and charge distribution. A lattice mismatch <3% between TiO$_2$ (0 0 1) on WO$_3$ (0 0 2) without dangling bonds, prefers to hetero-epitaxial growth of TiO$_2$ on WO$_3$, improving the photocorrosion of WO$_3$ for the high corrosion resistance and stability of TiO$_2$. The calculated valence band offset

(VBO) is 0.51 eV, forming a built-in field of TiO$_2$/WO$_3$ heterojunction from the staggered band alignment structure to inhibit the bulk charge recombination. With the introduction of CQDs, the bandgap is decreased from the density of states (DOS) indicating enhancing light harvesting, and charge transfer kinetics is promoted through the charge density difference. The designed CQDs/TiO$_2$/WO$_3$ photoanode significantly increases the photocurrent density from 0.90 to 2.03 mA cm^{-2} at 1.23 V, promotes charge separation efficiency from 56.3 to 79.2% and charge injection efficiency from 51.2 to 70.4%, and enhances the visible light absorption with better photostability and lower holes-to-water resistance.

2. Computational and experimental section

2.1. Computational details

The Vienna ab initio simulation package (VASP) is implemented with the projector augment wave (PAW) method for geometry structure optimization, band structure, charge density difference, Bader charge analysis and DOS [41,42]. The exchange–correlation function was treated through the generalized gradient approximation (GGA) of the PBE functional. The on-site correlation corrections were carried by the Hubbard model (DFT + U approach), and the value of the correlation energy (U) was set to 6.2 eV for the W, with a van der Waals interaction by the DFT-D2 method of Grimme [43]. The Kohn-Sham equations were solved with a plane wave basis set to self-consistency, with a convergence criteria of 10^{-4} eV and 0.015 eV Å^{-1} for energy and force. $4 \times 4 \times 4$ and $4 \times 4 \times 1$ gamma-centered k-space grid are used for the conventional cell and the slab model (15 Å vacuum layer), with the cutoff energy of 450 eV.

The VBO and conduction band offset (CBO) are computed on the basis of potential-line-up method [25], and the macroscopic average of the electrostatic potential of TiO$_2$/WO$_3$ are obtained to align the energy band of WO$_3$ and TiO$_2$. The planar averaged potential $\bar{V}(z)$ was calculated by Eq. (1):

$$\bar{V}(z) = \frac{1}{A} \int V(\bar{r}) dxdy \tag{1}$$

where A is the area of the interface. The macroscopic average potential $\bar{\bar{V}}(z)$ is obtained by Eq. (2):

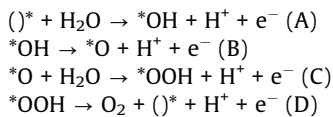$$\bar{\bar{V}}(z) = \frac{1}{L} \int_{-L/2}^{L/2} \bar{V}(z') dz' \tag{2}$$

where L is the period length. The VBO is calculated as Eq. (3):

$$\Delta E_{VBO} = \Delta \bar{\bar{V}}(z)_{TiO_2/WO_3} + (E_{VBM} - \bar{\bar{V}}(z))_{TiO_2} - (E_{VBM} - \bar{\bar{V}}(z))_{WO_3} \tag{3}$$

where $\Delta \bar{\bar{V}}(z)_{TiO_2/WO_3}$ is the difference of $\bar{\bar{V}}(z)$ between WO$_3$ and TiO$_2$. The E$_{VBM}$ and $\bar{\bar{V}}(z)$ are obtained from the conventional cells of WO$_3$ and TiO$_2$ [44].

The oxygen evolution reaction (OER) contains four proton transfer steps at the anode:

( )* + H_2O → *OH + H^+ + e^- (A)

*OH → *O + H^+ + e^- (B)

*O + H_2O → *OOH + H^+ + e^- (C)

OOH → O_2 + ( ) + H^+ + e^- (D)

where ( )* indicates the active site, and *OH, *O and *OOH are the intermediate of OER steps [45,46].

2.2. Synthesis of CQDs/TiO₂/WO₃ photoanode

The fluorine-doped tin oxide (FTO) substrate (7 Ω cm^{-1}) was ultrasonically cleaned with acetone, ethanol and deionized water (DI) for 0.5 h in turn. WO_3 nanoplates were hydrothermally synthesized in the precursor of 1 g ammonium paratungstate, 2 mL HCl (37%), 4 mL H_2O_2 (30%) and 93 mL DI at 160 °C for 4 h, and then were annealed in the air at 500 °C for 2 h to crystalline phase [12]. Subsequently, the anatase TiO_2 nanocones grow on WO_3 nanoplates by chemical bath deposition (CBD) that WO_3 film was dipped in the solution of 50 mM ammonium hexafluorotitanate and 150 mM boric acid at 25 °C for the different reaction time [47]. Finally CQDs were spin-coated twice on the TiO_2/WO_3 heterojunction by 1000 rpm for 10 s, and then was dried in air at 100 °C for 30 min. The CQDs solution is mixed with 50 mL glucose aqueous solution (62.5, 125, 250 and 500 mM) and 50 mL of NaOH (1 M) under ultrasonic treatment, and then is adjusted to pH = 7 with HCl and added equal volume of ethanol for agitating 1 h [16,48].

2.3. Material characterizations

The field emission scanning electron microscopy (FE-SEM) images were obtained by field emission scanning electron microscopy (Ultra Plus, Zeiss, Germany). The high-resolution transmission electronic microscopy (HRTEM) images and Selected Area Electron Diffraction (SAED) patterns were examined by Tecnai G2 F30 S-TWIN, FEI, USA. The crystalline phase was characterized by X-ray diffraction (XRD; AXS-8 Advance, Bruker, Germany). X-ray photoelectron spectrometry (XPS; AXIS Ultra DLD, Kratos, Japan) was used to analyze the elemental compositions and states. The light absorption spectra were measured by a UV–Vis spectrophotometer (TU1900, Beijing Purkinje General Instrument Co, China). Fourier transform infrared (FT-IR) spectroscopy were performed using IR/Nicolet 6700 (Thermo Fisher, America).

2.4. Photoelectrochemical measurements

Photoelectrochemical (PEC) measurements were carried out on an electrochemical workstation (CHI 660d, CH Instruments Inc., Shanghai) at room temperature in a 0.2 M Na_2SO_4 solution with a three-electrode optical cell. Illumination source was a 300 W Xe lamp with a power density of 100 mW cm^{-2} by an AM 1.5G solar power system. The photocurrent densities (J_{PEC}) were recorded by linear sweep voltammetry (LSV) under 50 mV s^{-1} scan rate. The potential versus Ag/AgCl ($E_{Ag/AgCl}$) were converted to the reversible hydrogen electrode (RHE) in Eq. (4):

$$E_{RHE} = E_{Ag/AgCl} + 0.0591\ V\ \times\ pH + 0.1976. \tag{4}$$

The incident photon-to-current efficiency (IPCE) was recorded under a 500 W Xe lamp (Zolix, China) with a monochromatic wavelength from 300 to 550 nm. Electrochemical impedance spectroscopy (EIS) was performed from 100 kHz to 0.1 Hz under illumination with amplitude perturbations of 5 mV. Intensity-modulated photocurrent spectroscopy (IMPS) were implemented on the electrochemical workstation (Zennium; effect-Eletrik, Germany) with the intensity-modulate photospectroscopy module (CIMPS, PP211) and a white-light lamp (WLC02; Zahner-Elektrik) from 0.1 Hz to 10 kHz. The transient photocurrent (TPC) was using a laser pulse (10 Hz, NT342A-10, EKSPLA) and a white-light lamp (WLC02; Zahner-Elektrik) on the electrochemical workstation (Zennium; effect-Eletrik, Germany).

3. Results and discussion

3.1. DFT theoretical calculations

The alignment of lattice parameter and energy band, and charge distribution in CQDs/TiO₂/WO₃ photoanode were obtained by DFT calculations. According to the computational results, TiO_2/WO_3 heterojunction was designed with the geometry optimization for WO_3 and TiO_2 conventional cells. In Fig. 1a and b, the optimized lattice parameters were a, b, c = 7.719, 7.680, 7.751 Å for WO_3, and a, b, c = 3.776, 3.776, 9.584 Å for anatase TiO_2, in accordance with the experimental values [49,50]. WO_3 (0 0 2) surface was chosen as the substrate according to our previous work [5], and three anatase TiO_2 (0 0 1), (1 0 1) and (1 0 0) facets are taken to construct the possible heterojucnction in Fig. S1 [35,51]. Studies have reported that the surface energies are 0.90, 0.53 and 0.44 J m^{-2} for (0 0 1), (1 0 0) and (1 0 1); therefore, the (1 0 1) facets are most stable than the others, and (0 0 1) facets show the best photocatalytic performance [18,52]. The mismatches between WO_3 (0 0 2) substrate and three abovementioned facets are listed in Table S1, where the minimum is that of TiO_2 (0 0 1). Therefore, the anatase TiO_2 could epitaxially grow along (0 0 1) orientation on the WO_3 (0 0 2) facet to construct the reasonable heterojucnction without dangling bonds in Fig. 1c [4].

The band structure of WO_3 and TiO_2 were calculated by the HSE06 hybrid function to explore the relation of band structures. In Fig. 1d, WO_3 is a direct bandgap semiconductor for the valence band maximum (VBM) and the conduction band minimum (CBM) both located at Γ point, with the calculated E_g of 2.88 eV close to the experimental value (2.72 eV) [5,53]. The anatase TiO_2 has an indirect bandgap of 3.47 eV close to the experimental value of 3.20 eV in Fig. 1e [54]. The electrostatic potentials of the TiO_2/WO_3 heterojunction, WO_3 and TiO_2 components are calculated to quantitate the band offset. The calculated difference of macroscopic average potential is 1.50 eV in Fig. S2. The VBO of the heterojunction is 0.51 eV according to Eq. (3), and the CBO is 1.11 eV in Fig. 1f. It is clear that TiO_2/WO_3 is a staggered band alignment structure, where the photoexcited holes in WO_3 transfer through the higher VBM of TiO_2 to oxide water, and the electrons in TiO_2 move to the lower CBM of WO_3 under the built-in field [55].

Additionally, the OER steps of the TiO_2/WO_3 heterojunction have been further investigated by DFT calculations. The interfacial OER is a four-proton transfer process with the Gibbs free energy change (ΔG) calculated by Eq. (5) [45]:

$$\Delta G\ (U, pH) = \Delta E + \Delta ZPE - T\Delta S - eU - k_B T\ \ln 10\ \times\ pH \tag{5}$$

where ΔE is the energy difference of products and reactants, ΔZPE represents the change in the zero-point energies (ZPEs), ΔS is the change in the entropy, and U is the external applied bias. The free energies of H_2O, H_2 and O_2 are displayed in Table S2 with the gaseous thermal correction, and free energies of intermediates are corrected by ZPEs in Tables S3 and S4. The pristine WO_3 surface terminated with oxygen atoms as the *O intermediate [46], initiates from reaction C to dissociate water molecules with *OOH. Subsequent reactions occur as the order of C-D-A-B with the cumulative reaction energy of each step in Fig. 2a. The maximum free energy difference of 3.67 eV is to release O_2 from *OOH, corresponding to the overpotential (η) of 2.44 V [56]. TiO_2/WO_3 heterojunction has the largest Gibbs free energy change of 2.89 eV (η = 1.66 V), limited by the H_2O adsroption to form *OH (Fig. 2b). Furthermore, CQDs modified on the surface of the heterojunction TiO_2/WO_3, has the
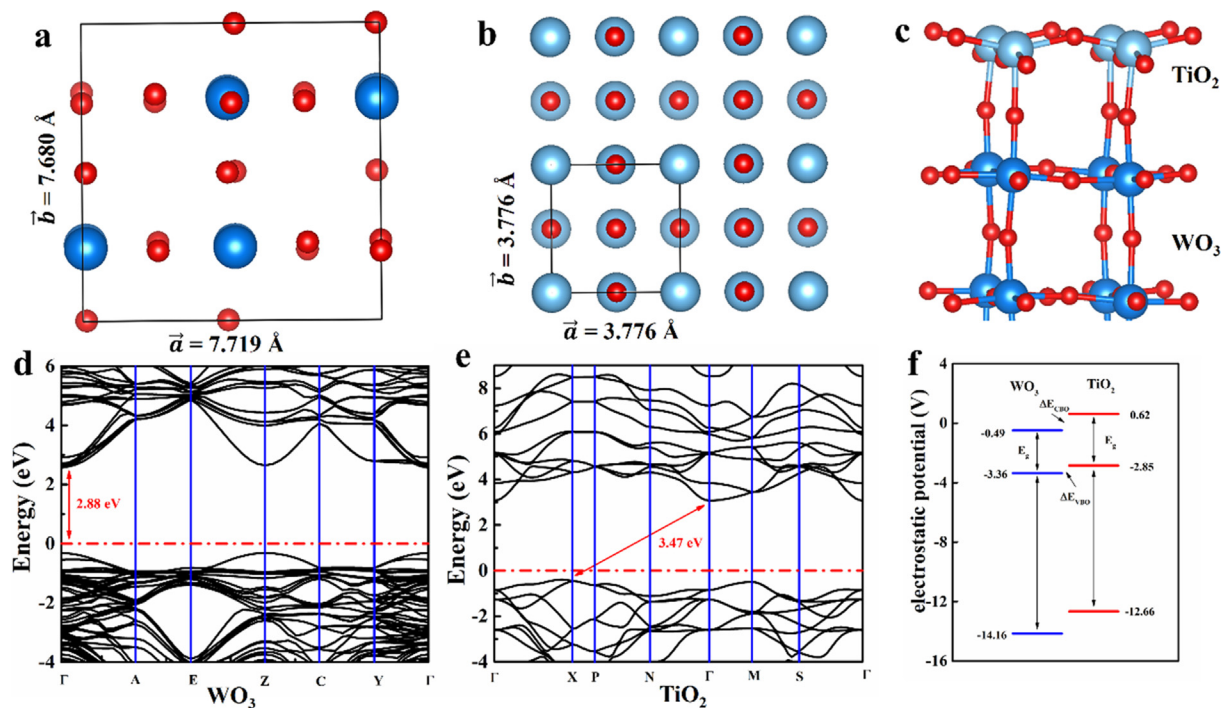
Fig. 1. (a) The top view of conventional cell of WO_3; (b) the top view of 2×2 unit of TiO_2; (c) the slab model of TiO_2/WO_3 heterojunction; (d–e) the band structures of WO_3 and TiO_2; and (f) the energy band offset of TiO_2/WO_3.
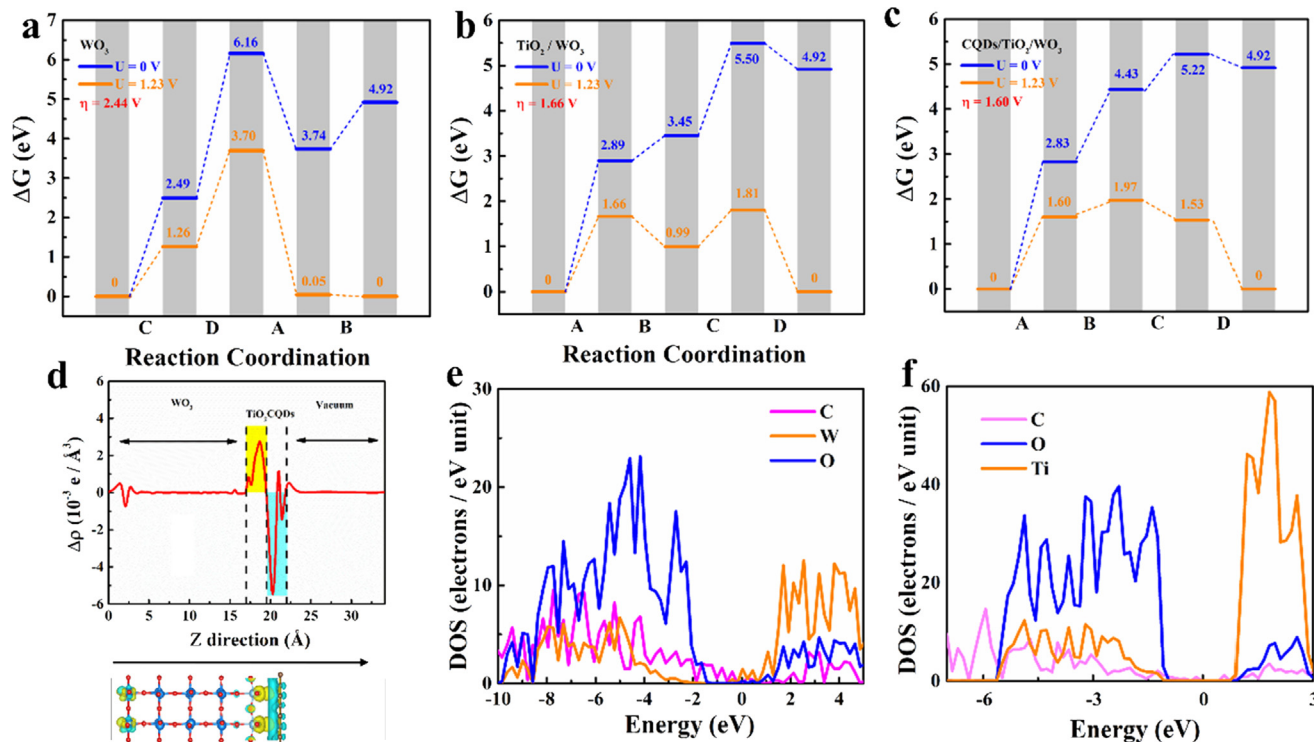

Fig. 2. (a–c) Gibbs free energy changes (ΔG) of OER process for WO_3, TiO_2/WO_3 and $CQDs/TiO_2/WO_3$; (d) planar-averaged electorn density difference for $CQDs/TiO_2$ along Z direction (The cyan indicates electron depletion and the yellow indicates electron accumulation); and (e–f) The DOS of $CQDs/WO_3$ and $CQDs/TiO_2$. (For interpretation of the references to colour in this figure legend, the reader is referred to the web version of this article.)

lowest overpotential of 1.60 V (Fig. 2c) in contrast to that of TiO_2/WO_3 and WO_3. Therefore the CQDs could further lower the overpotential of the TiO_2/WO_3 heterojunction to oxidize water molecules. The planar-averaged charge density difference is calculated at the

$CQDs/TiO_2/WO_3$ interface to reflect the charge distribution and transfer in Fig. 2d. The cyan area implies the charge depletion and the yellow area implies the charge accumulation, indicating that the photogenerated electrons transfer from CQDs to TiO_2, and the

holes inversely move to the semiconductor/electrolyte interface to oxidize water molecules. To quantify the charge change and transfer, the Bader charge of 0.161 e exchanges at the interface between CQDs and TiO_2. Through the charge density difference and the Bader charge analysis, it indicates that the loaded CQDs on TiO_2/WO_3 could accelerate photogenerated charge carriers transferring at the interfaces of semiconductor/electrolyte and CQDs/TiO_2. In Fig. 2-e-f, the calculated DOS of CQDs/WO_3 and CQDs/TiO_2 has shown the states of C element occupying the E_g of WO_3 and TiO_2; therefore CQDs may extended the wavelength of absorption edge to sufficiently utilize solar light [37].

3.2. Photoanode synthesis and characterization

To verify the calculations, the CQDs/TiO_2/WO_3 photoanode has been synthesized in Section 2.2, and the process is briefly illustrated as Fig. 3a. The morphology of WO_3 is nanoplates with the size ~2000 × 500 nm in the FE-SEM images (Fig. 3b). In Fig. 3c, the SEM image of TiO_2/WO_3 confirms that anatase TiO_2 has successfully grown on WO_3 nanoplates in the shape of nanocones by a chemical bath deposition (CBD) method [47]. And the photocurrent density of different CBD time of TiO_2 has been optimized to 30 min from Fig. S3, because the thicker TiO_2 may decay the photo
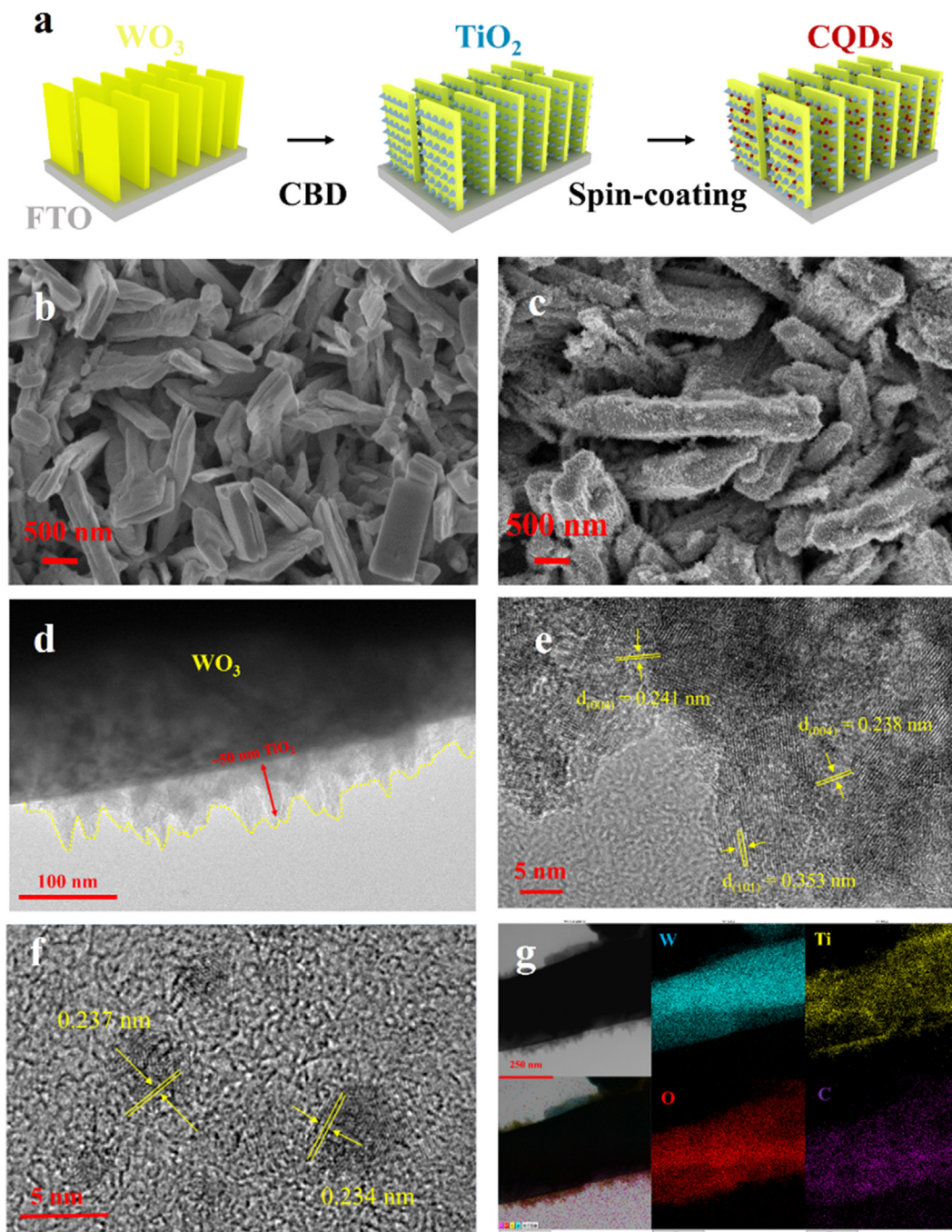

Fig. 3. (a) The process of preparing CQDs/TiO_2/WO_3 photoanode; (b) FE-SEM image of WO_3 nanoplates; (c) FE-SEM image of TiO_2/WO_3; (d-e) HRTEM images of TiO_2/WO_3 in different scales; (f) HRTEM image of CQDs; and (g) element mapping of CQDs/TiO_2/WO_3 in HRTEM.

harvesting of WO_3 substrate. From the HRTEM in Fig. 3d, the length of uniform TiO_2 nanocones is ~50 nm overlaying on WO_3 nanoplates. In Fig. 3e, the lattice spacing of 0.353 nm corresponds to anatase (101) facet [54,57], and 0.241 and 0.238 nm is for (004) plane indicating TiO_2 most in (001) orientation [4]. The XRD patterns (Fig. S4) have shown the characteristic peaks of different planes in the WO_3 crystalline structure (PDF#43–1035), consistent with the SAED pattern (Fig. S5) in the intensity of crystalline planes. There are no characteristic peaks of CQDs and TiO_2 in XRD for the low contents. CQDs are spin-coated on TiO_2/WO_3 with different layers and different concentrations to realize the maximum photocurrent density (Figs. S6-S7), and FE-SEM image shows a rough layer covered on the photoanode (Fig. S8). The HRTEM image of CQDs in Fig. 3f indicates that the planar distance of 0.237 and 0.234 nm corresponds to the (100) orientation of graphite [48,58]. In Fig. 3g, the Ti element is situated on the external layer of WO_3 consistent to the HRTEM image, and the distributed C element suggests CQDs coating on the photoanode (the element content of W, O, Ti and C shown in Table S5).

The XPS high-resolution spectra of Ti 2p for TiO_2/WO_3 (Fig. S9) indicates TiO_2 with the peaks at 458.3 eV and 463.9 eV [17,59]. And the total XPS of CQDs/TiO_2/WO_3 (Fig. S10) confirms the existence and the valence of elements in Fig. 3g. There are two kinds of oxygen chemical state observed for the O 1s XPS of the four samples in Fig. 4a, where the binding energy of 530.2–531.3 eV corresponds to lattice oxygen (O_L) and 531.9–532.5 eV corresponds chemical absorbed oxygen (O_C) [16,54]. With the loaded CQDs on WO_3 and TiO_2/WO_3, the peaks of O_L shifting to higher binding energy, is

attributed to the new binding between O-W or O-Ti and C [60,61]. Additionally, the peaks of O_c are intensified obviously and shifted to higher binding energy, indicating the increased content of O_c and decreased electron density of WO_3 and TiO_2/WO_3, with the introduction of CQDs for the additional C—O or C—OH groups [16]. The W 4f XPS spectra is shown in Fig. S11 with the peaks shifted to the lower binding energy with the introduction of CQDs, indicating the existence of W^{5+} and the formation of C—O [62]. In the C 1s XPS of CQDs/TiO_2/WO_3 (Fig. 4b), three peaks at 286.0 and 288.1 eV correspond to the C—C, C—O, and O=C—O groups, confirming the combination of CQDs and TiO_2/WO_3 [63,64]. In addition, the FT-IR spectra have shown the peak of C—O at 1057 cm^{-1} in Fig. S12, consistent with W 4f XPS spectra (Fig. S11) [17]. The VBM XPS spectra of TiO_2 and WO_3 is shown in Fig. S13, where the measured VBO is 0.59 eV, close to the calculated value (0.51 eV) in Fig. 1f.

The UV–Vis absorption spectra were measured over the wavelength range of 300–600 nm in Fig. 4c. Anatase TiO_2 could improve the ultraviolet light harvesting for TiO_2/WO_3 photoanode at the wavelength from 300 to 400 nm. In addition, CQDs have extended the absorption edge from 455 to 463 nm, with more utilization of visible light serving as semiconductor nanoparticles. And the CQDs/TiO_2/WO_3 has the best photo-response property associating the advantages of TiO_2 and CQDs. The Tauc plots could illustrate the energy bandgap (E_g) of photoanodes in Fig. 4d, where CQDs/TiO_2/WO_3 and CQDs/WO_3 have the closer E_g of 2.68 eV than 2.72 eV of TiO_2/WO_3 and WO_3 extending the visible absorption, consistent with the calculated DOS in Fig. 2d [37].
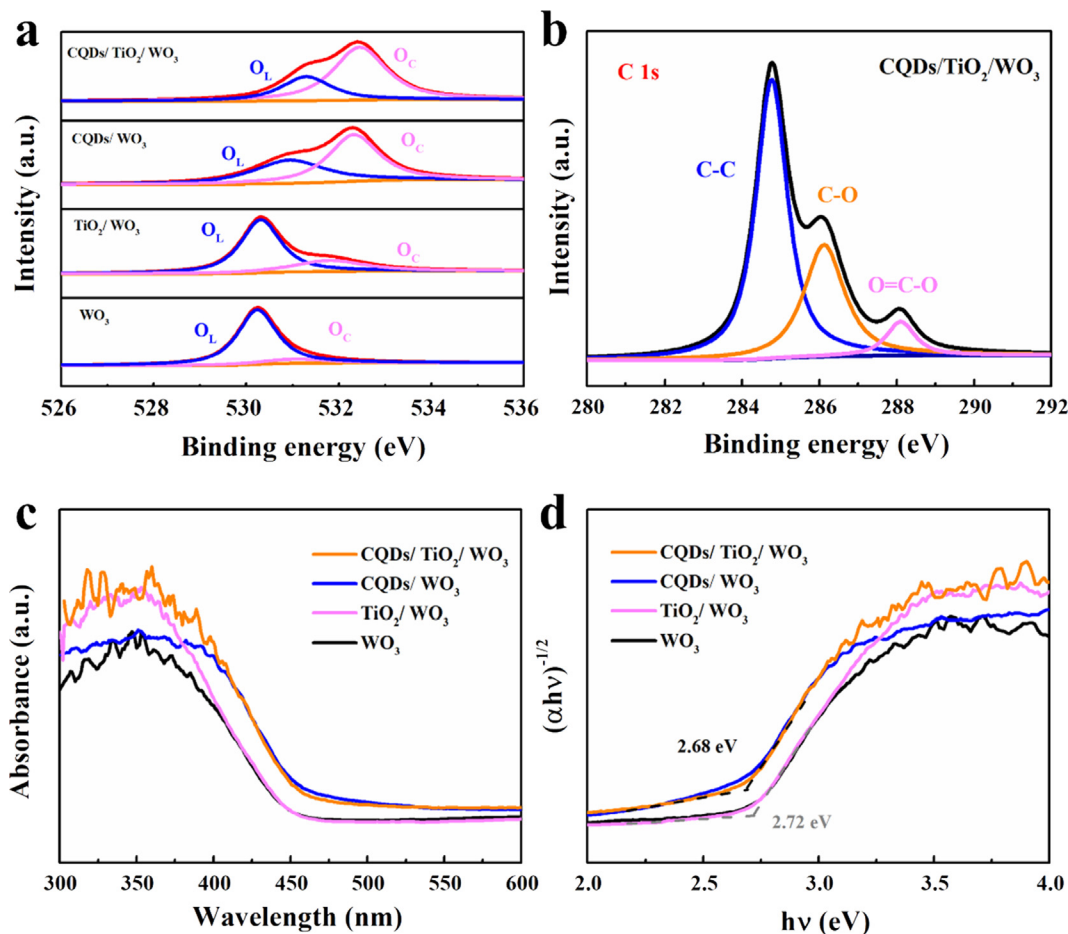

Fig. 4. (a) deconvoluted high-resolution O 1s XPS spectra of WO_3, TiO_2/WO_3, CQDs/WO_3 and CQDs/TiO_2/WO_3; (b) deconvoluted high-resolution C 1s spectrum of CQDs/TiO_2/WO_3; (c) UV–Vis absorption spectra and (d) Tauc plots for WO_3, CQDs/WO_3, TiO_2/WO_3 and CQDs/TiO_2/WO_3;
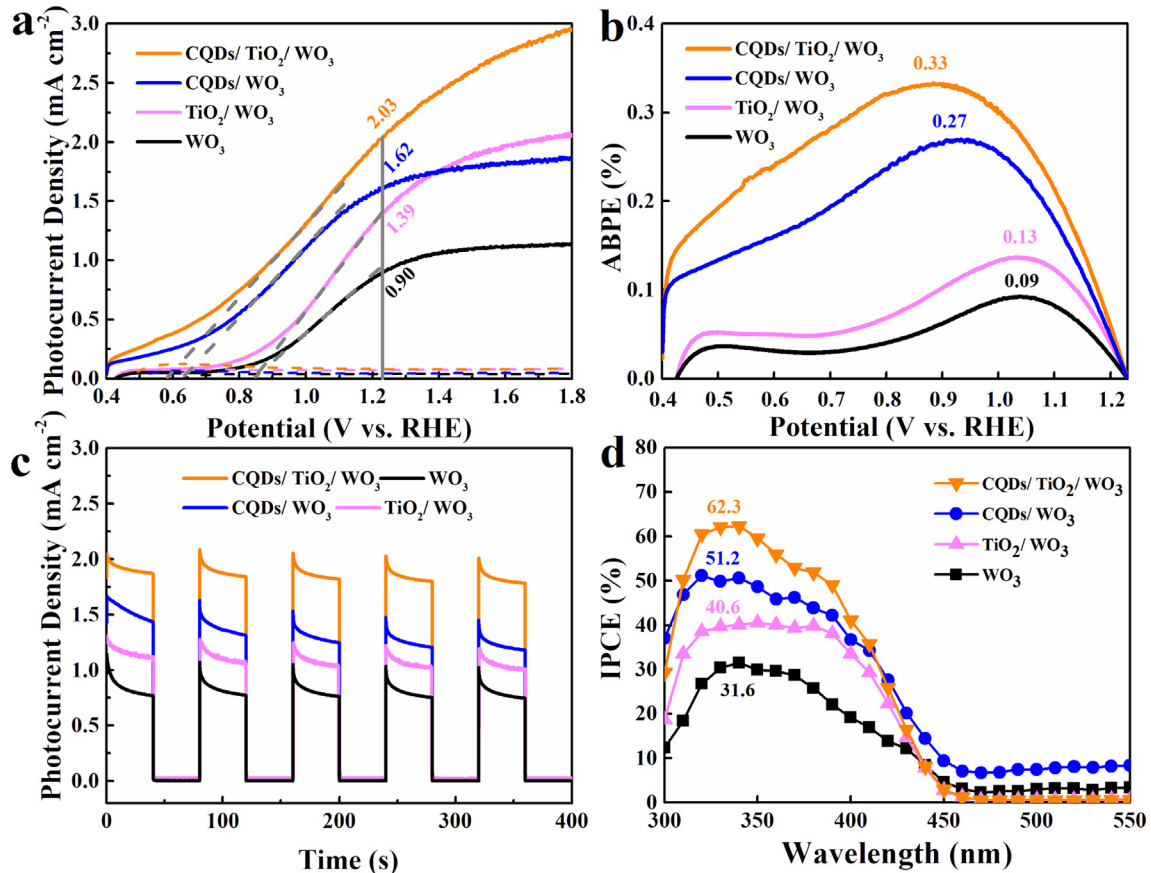
Fig. 5. (a) LSV curves, and (b) ABPE plots under a 0.2 M Na_2SO_4 aqueous solution; (c) CLV curves, and (d) IPCE plots at 1.23 V with 100 mW cm^{-2} irradiation for WO_3, TiO_2/WO_3, $CQDs$/WO_3 and $CQDs$/TiO_2/WO_3.

3.3. Experimental evaluation of PEC properties

In Fig. 5a, the photocurrent densities of TiO_2/WO_3, $CQDs$/WO_3 and $CQDs$/TiO_2/WO_3 photoanodes are 1.39, 1.62 and 2.03 mA cm^{-2} at 1.23 V *vs.* RHE, 1.54, 1.80 and 2.26 times than that of WO3 (0.90 mA cm^{-2}), with negligible dark current. In addition, CQDs have cathodically shifted 215 mV of onset potential over that of WO_3, but TiO_2 has no effect on onset potential with a rapid increasing current density. And the chopped photocurrent density curves of TiO_2 and $CQDs$/TiO_2 are shown in Fig. S14, where the CQDs could also improve the PEC performance of TiO_2. Therefore, the PEC improvement of $CQDs$/TiO_2/WO_3 is assigned to the synergistic impact of TiO_2/WO_3 heterojunction and CQDs oxygen evolution catalyst (OEC). The applied bias photon-to-current conversion efficiency (ABPE) are calculated from Eq. (6):

$$ABPE\ (\%) = (J \times (1.23 - V_b)/P_{tot}) \times 100\% \tag{6}$$

where J is the photocurrent density at V_b of LSV curves, and P_{tot} is the total power density of irradiation. As shown in Fig. 5b, the maximum ABPE of WO_3 and TiO_2/WO_3 reach 0.09% and 0.13% at ~1.05 V, while those of $CQDs$/WO_3 and $CQDs$/TiO_2/WO_3 get 0.27% and 0.33% at a lower potential ~0.9 V.

The chopped linear voltammery (CLV) were measured at 1.23 V with interval illumination in Fig. 5c. There are sharp transient spikes of the pristine WO_3 with the light switching on, indicating that the photogenerated holes accumulating and recombining on the surface rather than oxidizing water molecules. And the transient spikes abate for TiO_2/WO_3, $CQDs$/WO_3 and $CQDs$/TiO_2/WO_3, because the heterojunction and CQDs can efficiently suppress the recombination and accelerate the transfer of holes. The IPCE was

measured as a function of the incident light wavelength (300 ~ 550 nm) and calculated as Eq. (7):

$$IPCE\ (\%) = (1240 \times J_{mono})/(P_{mono} \times \lambda) \tag{7}$$

where J_{mono} is the recorded photocurrent density and P_{mono} is the measured light power density at the wavelength (λ) of incident light. In Fig. 5d, the maximum values of IPCE for WO_3, TiO_2/WO_3, $CQDs$/WO_3 and $CQDs$/TiO_2/WO_3 are 31.6, 40.6, 51.2 and 62.3% at ~ 340 nm. Moreover, TiO_2/WO_3 has better PEC stability with retaining 48.2% of initial photocurrent after 20000 s measurement, in contrast to that of 28.0% for pristine WO_3 in (Fig. S15). Tafel curves of $CQDs$/TiO_2/WO_3, TiO_2/WO_3 and WO_3 are shown in Fig. S16, pointing out the lowest overpotential of 303 mA dec^{-1} for $CQDs$/TiO_2/WO_3, in agreement with the DFT calculations (Fig. 2a–c).

3.4. Charge carrier transfer kinetics

The charge separation and transfer behaviours are studied to figure out the improved PEC performance of $CQDs$/TiO_2/WO_3. The photocurrent density in 0.2 M Na_2SO_4 (J_{PEC}) can be calculated from Eq. (8) [16,65]

$$J_{PEC} = J_{abs} \times \eta_{bulk} \times \eta_{surface} \tag{8}$$

where J_{abs} is estimated with 100% conversion of absorbed photons to current, η_{bulk} is the bulk efficiency of holes separating and transferring to the photoanode surface, and $\eta_{surface}$ is the surface efficiency of holes injecting and oxidizing water molecules at the semiconductor/electrolyte interface. The J_{abs} can be calculated to 3.11, 3.14, 3.66 and 3.71 mA cm^{-2} for WO_3, TiO_2/WO_3, $CQDs$/WO_3
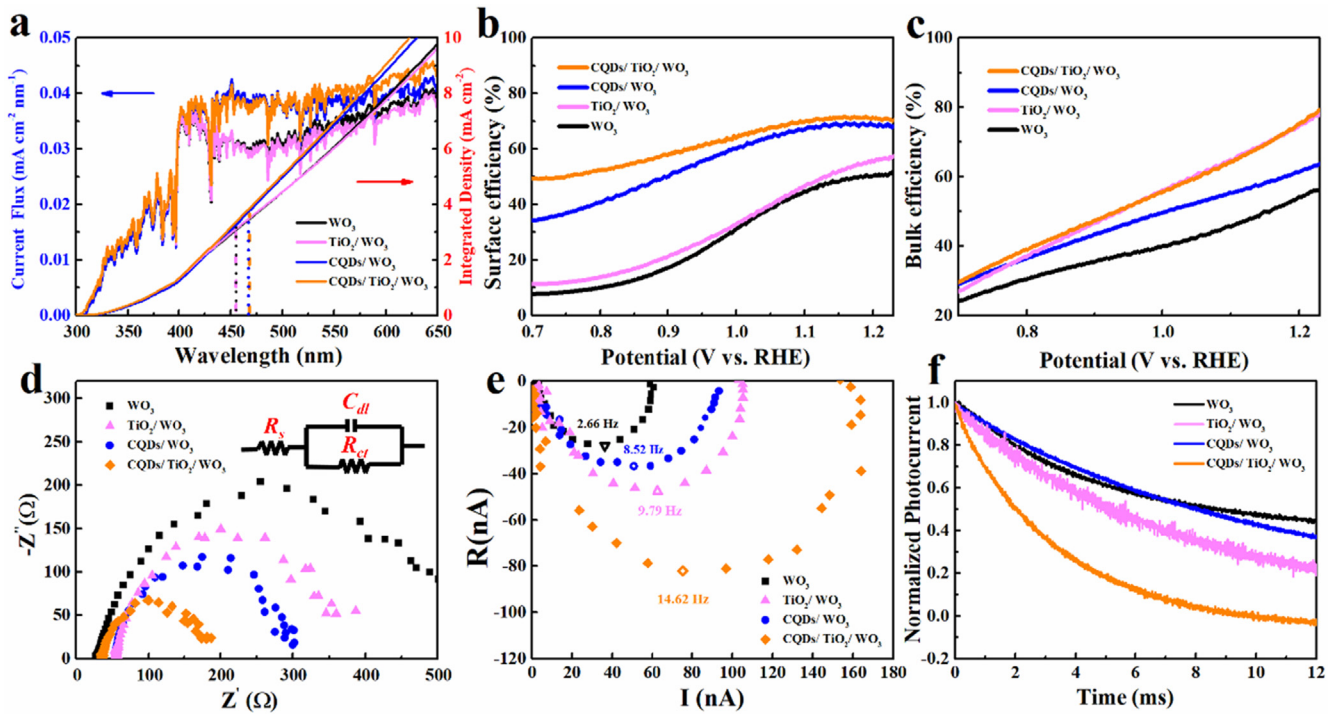
Fig. 6. (a) The calculated photocurrent flux and the integrated current densities, (b) surface injection efficiency, (c) bulk separation efficiencies, (d) EIS Nyquist plots under 100 mW cm^{-2}, (e) IMPS Nyquist plots, and (f) TPC curves for WO$_3$, CQDs/WO$_3$, TiO$_2$/WO$_3$ and CQDs/TiO$_2$/WO$_3$.

and CQDs/TiO$_2$/WO$_3$ in Fig. 6a, according to the AM 1.5G solar spectrum and light harvesting efficiency (LHE) [66,67]. It assumes that photogenerated holes will oxidize water molecules as soon as reaching the photoanode surface with hole scavenger (Na$_2$SO$_3$), namely suppressing surface recombination completely ($\eta_{surface}$ = 100%). Therefore $\eta_{surface}$ and η_{bulk} are calculated as Eqs. (9) and (10):

$$\eta_{surface} \approx J_{PEC}/J_{Na_2SO_3} \qquad (9)$$

$$\eta_{bulk} \approx J_{Na_2SO_3}/J_{abs} \qquad (10)$$

where J_{Na2SO3} and J_{PEC} are measured with or without Na$_2$SO$_3$. In Fig. 6b, the $\eta_{surface}$ of CQDs/TiO$_2$/WO$_3$ and CQDs/WO$_3$ are 70.4 and 68.0% at 1.23 V, much higher than 57.4% of TiO$_2$/WO$_3$ and 51.2% of WO$_3$. In Fig. 6c, η_{bulk} of TiO$_2$/WO$_3$ (78.0%) is approaching to that of CQDs/TiO$_2$/WO$_3$ (79.2), higher than 63.6 and 56.3% of CQDs/WO$_3$ and WO$_3$. It is obvious that $\eta_{surface}$ and η_{bulk} are significantly increasing after the modifications of CQDs and TiO$_2$ over pristine WO$_3$.

EIS, IMPS and TPC were carried out to further explore the roles of CQDs and TiO$_2$ on charge transfer kinetics. In Fig. 6d, the semi-circle radii of the EIS Nyquist plot follow the order: WO$_3$ > TiO$_2$/WO$_3$ > CQDs/WO$_3$ > CQDs/TiO$_2$/WO$_3$, charactering the holes-to-water resistance at the semiconductor/electrolyte interface [67,68]. The inset of Fig. 6d is a Randle equivalent circuit fitted by ZSimpWin, with the systemic series resistance R$_s$, the interfacial charge transfer resistance R$_{ct}$, and the capacitance of the double layer C$_{dl}$ listed in the Table S6. The minimum R$_{ct}$ is 153.5 Ω of CQDs/TiO$_2$/WO$_3$, indicating lowest interfacial charge transfer resistance for holes-to-water [69,70]. The fitted R$_{ct}$ of CQDs/WO$_3$ is 233.8 Ω smaller than that of TiO$_2$/WO$_3$ (297.1 Ω), pointing out that CQDs are better at carriers surface injection than TiO$_2$, in accordance with the surface efficiencies (Fig. 6b).

The electron collection time τ_c represents the average time of electrons transferring from the semiconductor to the substrate, and is derived as Eq. (11) [71]:

$$\tau_c = 1/2\pi f_{min} \qquad (11)$$

where f_{min} is the frequency of minimum imaginary value of IMPS Nyquist plots in Fig. 6e. The obtained frequency of minimum imaginary values correspond to the τ_c of 59.9, 18.7, 16.2 and 10.9 ms for WO$_3$, CQDs/WO$_3$, TiO$_2$/WO$_3$ and CQDs/TiO$_2$/WO$_3$, which owns the quickest electrons transfer kinetics. The TPC could reflect the time τ_t of charge carriers transferring from the photoanodes to the substrate in Fig. 6f, by bi-exponential fitting (Table S7) [72]. The calculated τ_t of CQDs/TiO$_2$/WO$_3$ is 3.41 ms much less than 13.28 (WO$_3$), 11.34 (CQDs/WO$_3$) and 7.37 ms (TiO$_2$/WO$_3$), demonstrating that photogenerated electrons separate from the photoanode and transfer to the FTO rapidly, consistent with the bulk efficiencies (Fig. 6c) and the IMPS plots (Fig. 6e). Therefore, the charge transfer kinetics of CQDs/TiO$_2$/WO$_3$ could be accelerated with the loading of TiO$_2$ and CQDs [37].

4. Conclusion

In summary, the theoretical calculations reveal the dual alignment of lattice parameters and band structures for the epitaxial heterojuction TiO$_2$/WO$_3$, and the improved electronic and optical properties with the introduction of CQDs. According to DFT results, the CQDs/TiO$_2$/WO$_3$ photoanode is designed and synthesized, to improve the photocurrent density to 2.03 mA cm^{-2} over 0.90 mA cm^{-2} for pristine WO$_3$ dramatically. Furthermore, the novel photoanode owns better photostability, higher charge separation and transfer, enhanced light absorption, and rapid reaction kinetics, for the synergetic effects of CQDs (visible light sensitizer) and TiO$_2$ (built-in field).

CRediT authorship contribution statement

Jiachen Wang: Conceptualization, Methodology, Investigation, Visualization, Formal analysis, Data curation, Validation, Writing - original draft, Writing - review & editing. **Tingsheng Zhou:** Investigation. **Yan Zhang:** Formal analysis, Validation. **Shuai Chen:** Formal analysis. **Jing Bai:** Supervision, Project administration, Resources, Funding acquisition. **Jinhua Li:** Investigation, Data curation. **Hong Zhu:** Resources, Supervision. **Baoxue Zhou:** Conceptualization, Resources, Supervision, Project administration, Writing - review & editing, Funding acquisition.

Declaration of Competing Interest

The authors declare that they have no known competing financial interests or personal relationships that could have appeared to influence the work reported in this paper.

Acknowledgements

Appendix A. Supplementary material

Supplementary data to this article can be found online at https://doi.org/10.1016/j.jcis.2021.05.086.

References

[1] M. Grätzel, Photoelectrochemical Cells, Nature 414 (2001) 338–344.

[2] Q. Zeng, J. Li, L. Li, J. Bai, L. Xia, B. Zhou, Synthesis of WO₃/BiVO₄ Photoanode Using a Reaction of Bismuth Nitrate with Peroxovanadate on WO₃ Film for Efficient Photoelectrocatalytic Water Splitting and Organic Pollutant Degradation, Appl. Catal. B 217 (2017) 21–29.

[3] S.V.P. Vattikuti, C. Byon, I. Ngo, Highly Crystalline Multi-Layered WO₃ Sheets for Photodegradation of Congo Red under Visible Light Irradiation, Mater. Res. Bull. 84 (2016) 288–297.

[4] Q. Zeng, J. Bai, J. Li, B. Zhou, Y. Sun, A Low-Cost Photoelectrochemical Tandem Cell for Highly-Stable and Efficient Solar Water Splitting, Nano Energy 41 (2017) 225–232.

[5] J. Wang, Y. Zhang, T. Zhou, S. Chen, H. Zhu, J. Bai, J. Li, B. Zhou, Efficient WO₃₋ₓ Nanoplates Photoanode Based on Bidentate Hydrogen Bonds and Thermal Reduction of Ethylene Glycol, Chem. Eng. J. 404 (2021) 127089.

[6] T. Zhou, J. Wang, S. Chen, J. Bai, J. Li, Y. Zhang, L. Li, L. Xia, M. Rahim, Q. Xu, B. Zhou, Bird-Nest Structured ZnO/TiO₂ as a Direct Z-Scheme Photoanode with Enhanced Light Harvesting and Carriers Kinetics for Highly Efficient and Stable Photoelectrochemical Water Splitting, Appl. Catal. B 267 (2020) 118599.

[7] S. Chen, J. Li, J. Bai, L. Xia, Y. Zhang, L. Li, Q. Xu, B. Zhou, Electron Blocking and Hole Extraction by a Dual-Function Layer for Hematite with Enhanced Photoelectrocatalytic Performance, Appl. Catal. B 237 (2018) 175–184.

[8] L. Xia, J. Li, J. Bai, L. Li, S. Chen, B. Zhou, BiVO₄ Photoanode with Exposed (040) Facets for Enhanced Photoelectrochemical Performance, Nano-Micro Letters 10 (2018) 11.

[9] X. Liu, F. Wang, Q. Wang, Nanostructure-Based WO₃ Photoanodes for Photoelectrochemical Water Splitting, PCCP 14 (2012) 7894–7911.

[10] C.A. Bignozzi, S. Caramori, V. Cristino, R. Argazzi, L. Meda, A. Tacca, Nanostructured Photoelectrodes Based on WO₃: Applications to Photooxidation of Aqueous Electrolytes, Chem. Soc. Rev. 42 (2013) 2228–2246.

[11] Q. Mi, A. Zhanaidarova, B.S. Brunschwig, H.B. Gray, N.S. Lewis, A Quantitative Assessment of the Competition between Water and Anion Oxidation at WO₃ Photoanodes in Acidic Aqueous Electrolytes, Energy Environ. Sci. 5 (2012) 5694–5700.

[12] S.S. Kalanur, Y.J. Hwang, S.Y. Chae, O.S. Joo, Facile Growth of Aligned WO₃ Nanorods on FTO Substrate for Enhanced Photoanodic Water Oxidation Activity, J. Mater. Chem. A 1 (2013) 3479–3488.

[13] G. Zheng, J. Wang, H. Liu, V. Murugadoss, G. Zu, H. Che, C. Lai, H. Li, T. Ding, Q. Gao, Z. Guo, Tungsten Oxide Nanostructures and Nanocomposites for Photoelectrochemical Water Splitting, Nanoscale 11 (2019) 18968–18994.

[14] J.C. Hill, K.S. Choi, Effect of Electrolytes on the Selectivity and Stability of n-type WO₃ Photoelectrodes for Use in Solar Water Oxidation, J. Phys. Chem. C 116 (2012) 7612–7620.

[15] K. Fuku, N. Wang, Y. Miseki, T. Funaki, K. Sayama, Photoelectrochemical Reaction for the Efficient Production of Hydrogen and High-Value-Added Oxidation Reagents, ChemSusChem 8 (2015) 1593–1600.

[16] T. Zhou, S. Chen, L. Li, J. Wang, Y. Zhang, J. Li, J. Bai, L. Xia, Q. Xu, M. Rahim, B. Zhou, Carbon Quantum Dots Modified Anatase/Rutile TiO₂ Photoanode with Dramatically Enhanced Photoelectrochemical Performance, Appl. Catal. B 269 (2020) 118776.

[17] A.K.R. Police, M. Chennaiahgari, R. Boddula, S.V.P. Vattikuti, K.K. Mandari, B. Chan, Single-Step Hydrothermal Synthesis of Wrinkled Graphene Wrapped TiO₂ Nanotubes for Photocatalytic Hydrogen Production and Supercapacitor Applications, Mater. Res. Bull. 98 (2018) 314–321.

[18] A.K.R. Police, S.V.P. Vattikuti, Y.-J. Baik, B. Chan, Eco-Friendly, Hydrogen Fluoride-Free, Morphology-Oriented Synthesis of TiO₂ with Exposed (001) Facets, Ceram. Int. 45 (2019) 2178–2184.

[19] Y. Wang, W. Tian, L. Chen, F. Cao, J. Guo, L. Li, Three-Dimensional WO₃ Nanoplate/Bi₂S₃ Nanorod Heterojunction as a Highly Efficient Photoanode for Improved Photoelectrochemical Water Splitting, ACS Appl. Mater. Interfaces 9 (2017) 40235–40243.

[20] Y. Fu, Z. Ren, J. Wu, Y. Li, W. Liu, P. Li, L. Xing, J. Ma, H. Wang, X. Xue, Direct Z-Scheme Heterojunction of ZnO/MoS₂ Nanoarrays Realized by Flowing-Induced Piezoelectric Field for Enhanced Sunlight Photocatalytic Performances, Appl. Catal. B 285 (2021) 119785.

[21] K.C. Leonard, K.M. Nam, H.C. Lee, S.H. Kang, H.S. Park, A.J. Bard, ZnWO₄/WO₃ Composite for Improving Photoelectrochemical Water Oxidation, J. Phys. Chem. C 117 (2013) 15901–15910.

[22] S. Le, T. Jiang, Y. Li, Q. Zhao, Y. Li, W. Fang, M. Gong, Highly Efficient Visible-Light-Driven Mesoporous Graphitic Carbon Nitride/ZnO Nanocomposite Photocatalysts, Appl. Catal. B 200 (2017) 601–610.

[23] A.K.R. Police, S.V.P. Vattikuti, M. Chennaiahgari, P.S. M.V, D.K. Valluri, C. Byon, Bismuth Oxide Cocatalyst and Copper Oxide Sensitizer in Cu2O/TiO2/Bi2O3 Ternary Photocatalyst for Efficient Hydrogen Production under Solar Light Irradiation, Ceram. Int. 44 (2018) 11783–11791.

[24] J. Zhang, W. Wang, N. Wang, M. Wang, Y. Qi, Atomic-Resolution Study on the Interface Structure and Strain State Reversion of the Bi₂Sr₂CuO₆₊δ/MgO Heterostructure, J. Colloid Interface Sci. 592 (2021) 291–295.

[25] N.R. D'Amico, G. Cantele, D. Ninno, First Principles Calculations of the Band Offset at SrTiO₃₋TiO₂ Interfaces, Appl. Phys. Lett. 101 (2012) 141606.

[26] X. Ma, Y. Wei, Z. Wei, H. He, C. Huang, Y. Zhu, Probing Pi-Pi Stacking Modulation of g-C₃N₄/Graphene Heterojunctions and Corresponding Role of Graphene on Photocatalytic Activity, J. Colloid Interface Sci. 508 (2017) 274–281.

[27] T. Zhou, S. Chen, J. Wang, Y. Zhang, J. Li, J. Bai, B. Zhou, Dramatically Enhanced Solar-Driven Water Splitting of BiVO4 Photoanode via Strengthening Hole Transfer and Light Harvesting by Co-Modification of CQDs and Ultrathin β-FeOOH Layers, Chem. Eng. J. 403 (2021) 126350–126362.

[28] S.Y. Lim, W. Shen, Z. Gao, Carbon Quantum Dots and Their Applications, Chem. Soc. Rev. 44 (2015) 362–381.

[29] J. Shen, Y. Zhu, C. Chen, X. Yang, C. Li, Facile Preparation and Upconversion Luminescence of Graphene Quantum Dots, Chem. Commun. 47 (2011) 2580–2582.

[30] H. Yu, Y. Zhao, C. Zhou, L. Shang, Y. Peng, Y. Cao, L.-Z. Wu, C.-H. Tung, T. Zhang, Carbon Quantum Dots/TiO₂ Composites for Efficient Photocatalytic Hydrogen Evolution, J. Mater. Chem. A 2 (2014) 3344–3351.

[31] Y. Zeng, D. Chen, T. Chen, M. Cai, Q. Zhang, Z. Xie, R. Li, Z. Xiao, G. Liu, W. Lv, Study on Heterogeneous Photocatalytic Ozonation Degradation of Ciprofloxacin by TiO₂/Carbon Dots: Kinetic, Mechanism and Pathway Investigation, Chemosphere 227 (2019) 198–206.

[32] X. Ju, J. Huang, F. Zhao, P. Yi, B. He, Y. Wang, T. Chen, Y. Chen, Z. Li, X. Liu, Photothermal Effect of Carbon Quantum Dots Enhanced Photoelectrochemical Water Splitting of Hematite Photoanodes, J. Mater. Chem. A 8 (2020) 14915–14920.

[33] Z. Zhao, T. Butburee, P. Peerakiatkhajohn, M. Lyu, S. Wang, L. Wang, H. Zheng, Carbon Quantum Dots Sensitized Vertical WO₃ Nanoplates with Enhanced Photoelectrochemical Properties, ChemistrySelect 1 (2016) 2772–2777.

[34] X. Xu, Z. Bao, W. Tang, H. Wu, J. Pan, J. Hu, H. Zeng, Surface States Engineering Carbon Dots as Multi-Band Light Active Sensitizers for ZnO Nanowire Array Photoanode to Boost Solar Water Splitting, Carbon 121 (2017) 201–208.

[35] Y. Hu, Y. Pan, Z. Wang, T. Lin, Y. Gao, B. Luo, H. Hu, F. Fan, G. Liu, L. Wang, Lattice Distortion Induced Internal Electric Field in TiO₂ Photoelectrode for Efficient Charge Separation and Transfer, Nat. Commun. 11 (2020) 2129.

[36] Q. Wang, J. Cai, G.V. Biesold-McGee, J. Huang, Y.H. Ng, H. Sun, J. Wang, Y. Lai, Z. Lin, Silk Fibroin-Derived Nitrogen-Doped Carbon Quantum Dots Anchored on TiO₂ Nanotube Arrays for Heterogeneous Photocatalytic Degradation and Water Splitting, Nano Energy 78 (2020) 105313–105327.

[37] X. Sun, W. He, T. Yang, H. Ji, W. Liu, J. Lei, Y. Liu, Z. Cai, Ternary TiO2/WO3/CQDs Nanocomposites for Enhanced Photocatalytic Mineralization of Aqueous Cephalexin: Degradation Mechanism and Toxicity Evaluation, Chem. Eng. J. 412 (2021) 128679.

[38] U.A. Rani, L.Y. Ng, C.Y. Ng, E. Mahmoudi, A Review of Carbon Quantum Dots and Their Applications in Wastewater Treatment, Adv. Colloid Interface Sci. 278 (2020) 102124.

[39] Z. Zhu, J. Ma, Z. Wang, C. Mu, Z. Fan, L. Du, Y. Bai, L. Fan, H. Yan, D.L. Phillips, S. Yang, Efficiency Enhancement of Perovskite Solar Cells through Fast Electron

Extraction: The Role of Graphene Quantum Dots, J. Am. Chem. Soc. 136 (2014) 3760–3763.

[40] X. Lv, X. Xiao, M. Cao, Y. Bu, C. Wang, M. Wang, Y. Shen, Efficient Carbon Dots/ NiFe-layered Double Hydroxide/BiVO$_4$ Photoanodes for Photoelectrochemical Water Splitting, Appl. Surf. Sci. 439 (2018) 1065–1071.

[41] G. Kresse, J. Furthmüller, Efficient Iterative Schemes for Ab Initio Total-Energy Calculations Using a Plane-Wave Basis Set, Phys. Rev. B 54 (1996) 11169–11186.

[42] G. Kresse, J. Furthmüller, Efficiency of Ab-Initio Total Energy Calculations for Metals and Semiconductors Using a Plane-Wave Basis Set, Comput. Mater. Sci. 6 (1996) 15–50.

[43] S. Grimme, Semiempirical GGA-Type Density Functional Constructed with a Long-Range Dispersion Correction, J. Comput. Chem. 27 (2006) 1787–1799.

[44] J. Liu, B. Cheng, J. Yu, A New Understanding of the Photocatalytic Mechanism of the Direct Z-Scheme g-C$_3$N$_4$/TiO$_2$ Heterostructure, PCCP 18 (2016) 31175–31183.

[45] Á. Valdés, Z.W. Qu, G.J. Kroes, J. Rossmeisl, J.K. Nørskov, Oxidation and Photo-Oxidation of Water on TiO$_2$ Surface, J. Phys. Chem. C 112 (2008) 9872–9879.

[46] P. Liao, J.A. Keith, E.A. Carter, Water Oxidation on Pure and Doped Hematite (0001) Surfaces: Prediction of Co and Ni as Effective Dopants for Electrocatalysis, J. Am. Chem. Soc. 134 (2012) 13296–13309.

[47] J.H. Lee, I.C. Leu, M.C. Hsu, Y.W. Chung, M.H. Hon, Fabrication of Aligned TiO$_2$ One-Dimensional Nanostructured Arrays Using a One-Step Templating Solution Approach, J. Phys. Chem. B 109 (2005) 13056–13059.

[48] W. Shi, X. Zhang, J. Brillet, D. Huang, M. Li, M. Wang, Y. Shen, Significant Enhancement of the Photoelectrochemical Activity of WO$_3$ Nanoflakes by Carbon Quantum Dots Decoration, Carbon 105 (2016) 387–393.

[49] T. Vogt, P.M. Woodward, B.A. Hunter, The High-Temperature Phases of WO$_3$, J. Solid State Chem. 144 (1999) 209–215.

[50] J.K. Burdett, T. Hughbanks, G.J. Miller, J.W. Richardson, J.V. Smith, Structural-Electronic Relationships in Inorganic Solids: Powder Neutron Diffraction Studies of the Rutile and Anatase Polymorphs of Titanium Dioxide at 15 and 295 K, J. Am. Chem. Soc. 109 (1987) 3639–3646.

[51] T. Mi, Y. Wu, X. Zhou, W. Li, L. Zhao, J. Liu, Q. Lu, Catalytic Oxidation of Co over V$_2$O$_5$/TiO$_2$ and V$_2$O$_5$-WO$_3$/TiO$_2$ Catalysts: A DFT Study, Fuel Process. Technol. 213 (2021) 106678.

[52] M. Lazzeri, A. Vittadini, A. Selloni, Structure and Energetics of Stoichiometric TiO$_2$ Anatase Surfaces, Phys. Rev. B 63 (2001) 155409.

[53] E. Albanese, C. Di Valentin, G. Pacchioni, H$_2$O Adsorption on WO$_3$ and WO$_{3-x}$ (001) Surfaces, ACS Appl. Mater. Interfaces 9 (2017) 23212–23221.

[54] J. Hu, S. Zhang, Y. Cao, H. Wang, H. Yu, F. Peng, Novel Highly Active Anatase/ Rutile TiO$_2$ Photocatalyst with Hydrogenated Heterophase Interface Structures for Photoelectrochemical Water Splitting into Hydrogen, ACS Sustainable Chem. Eng. 6 (2018) 10823–10832.

[55] J. Resasco, H. Zhang, N. Kornienko, N. Becknell, H. Lee, J. Guo, A.L. Briseno, P. Yang, TiO$_2$/BiVO$_4$ Nanowire Heterostructure Photoanodes Based on Type II Band Alignment, ACS Cent. Sci. 2 (2016) 80–88.

[56] Z. Wang, X. Mao, P. Chen, M. Xiao, S.A. Monny, S. Wang, M. Konarova, A. Du, L. Wang, Understanding the Roles of Oxygen Vacancies in Hematite-Based Photoelectrochemical Processes, Angew. Chem. Int. Ed. 58 (2019) 1030–1034.

[57] J. Tian, Y. Leng, Z. Zhao, Y. Xia, Y. Sang, P. Hao, J. Zhan, M. Li, H. Liu, Carbon Quantum Dots/Hydrogenated TiO$_2$ Nanobelt Heterostructures and Their Broad Spectrum Photocatalytic Properties under UV, Visible, and near-Infrared Irradiation, Nano Energy 11 (2015) 419–427.

[58] P. Luan, X. Zhang, Y. Zhang, Z. Li, U. Bach, J. Zhang, Dual Quantum Dot-Decorated Bismuth Vanadate Photoanodes for Highly Efficient Solar Water Oxidation, ChemSusChem 12 (2019) 1240–1245.

[59] S. Xie, H. Su, W. Wei, M. Li, Y. Tong, Z. Mao, Remarkable Photoelectrochemical Performance of Carbon Dots Sensitized TiO$_2$ under Visible Light Irradiation, J. Mater. Chem. A 2 (2014) 16365–16368.

[60] G. Wang, W. Zhang, J. Li, X. Dong, X. Zhang, Carbon Quantum Dots Decorated BiVO$_4$ Quantum Tube with Enhanced Photocatalytic Performance for Efficient Degradation of Organic Pollutants under Visible and near-Infrared Light, J. Mater. Sci. 54 (2019) 6488–6499.

[61] F. Ning, M. Shao, S. Xu, Y. Fu, R. Zhang, M. Wei, D.G. Evans, X. Duan, TiO$_2$/ Graphene/NiFe-layered Double Hydroxide Nanorod Array Photoanodes for Efficient Photoelectrochemical Water Splitting, Energy Environ. Sci. 9 (2016) 2633–2643.

[62] M. Ma, K. Zhang, P. Li, M.S. Jung, M.J. Jeong, J.H. Park, Dual Oxygen and Tungsten Vacancies on a WO$_3$ Photoanode for Enhanced Water Oxidation, Angew. Chem. Int. Ed. 55 (2016) 11819–11823.

[63] Z. Liang, H. Hou, Z. Fang, F. Gao, L. Wang, D. Chen, W. Yang, Hydrogenated TiO$_2$ Nanorod Arrays Decorated with Carbon Quantum Dots toward Efficient Photoelectrochemical Water Splitting, ACS Appl. Mater. Interfaces 11 (2019) 19167–19175.

[64] R. Miao, Z. Luo, W. Zhong, S. Chen, T. Jiang, B. Dutta, Y. Nasr, Y. Zhang, S.L. Suib, Mesoporous TiO$_2$ Modified with Carbon Quantum Dots as a High-Performance Visible Light Photocatalyst, Appl. Catal. B 189 (2016) 26–38.

[65] T.W. Kim, K.S. Choi, Nanoporous BiVO$_4$ Photoanodes with Dual-Layer Oxygen Evolution Catalysts for Solar Water Splitting, Science 343 (2014) 990–994.

[66] J.H. Kim, J.S. Lee, Elaborately Modified BiVO$_4$ Photoanodes for Solar Water Splitting, Adv. Mater. 31 (2019) e1806938.

[67] G. Yang, Y. Li, H. Pang, K. Chang, J. Ye, Ultrathin Cobalt-Manganese Nanosheets: An Efficient Platform for Enhanced Photoelectrochemical Water Oxidation with Electron-Donating Effect, Adv. Funct. Mater. 29 (2019) 1904622.

[68] K. Ye, Z. Wang, J. Gu, S. Xiao, Y. Yuan, Y. Zhu, Y. Zhang, W. Mai, S. Yang, Carbon Quantum Dots as a Visible Light Sensitizer to Significantly Increase the Solar Water Splitting Performance of Bismuth Vanadate Photoanodes, Energy Environ. Sci. 10 (2017) 772–779.

[69] K.G. Upul Wijayantha, S. Saremi Yarahmadi, L.M. Peter, Kinetics of Oxygen Evolution at Alpha-Fe$_2$O$_3$ Photoanodes: A Study by Photoelectrochemical Impedance Spectroscopy, PCCP 13 (2011) 5264–5270.

[70] A. Valdes, Z. Qu, G. Kroes, J. Rossmeisl, J.K. Nørskov, Oxidation and Photo-Oxidation of Water on TiO$_2$ Surface, J. Phys. Chem. C 112 (2008) 9872–9879.

[71] K. Zhu, N.R. Neale, A. Miedaner, A.J. Frank, Enhanced Charge-Collection Efficiencies and Light Scattering in Dye-Sensitized Solar Cells Using Oriented TiO$_2$ Nanotubes Arrays, Nano Lett. 7 (2007) 69–74.

[72] Y. Li, L. Meng, Y.M. Yang, G. Xu, Z. Hong, Q. Chen, J. You, G. Li, Y. Yang, Y. Li, High-Efficiency Robust Perovskite Solar Cells on Ultrathin Flexible Substrates, Nat. Commun. 7 (2016) 10214.